Computer-aided detection of wall motion abnormalities in cardiac MRI

Suinesiaputra, A.

2

Optic flow computation from cardiac MR tagging using a multiscale differential method: A comparative study with Velocity-Encoded MRI

Abstract

The computation of an optic flow field to reconstruct a dense velocity field from a sequence of tagged MR images faces a major difficulty: a non-constant pixel intensity. In this chapter, this problem was resolved by regarding the MRI sequence as density images, which adhere to a principle of conservation of intensity. Based on this principle, optic flow equations were developed based on Gaussian derivatives as differential operators. The multiscale optic flow method was applied to cardiac tagged MRI. A quantitative analysis is presented comparing the reconstructed dense velocity field with a directly acquired velocity field using the velocity-encoded (VEC) MRI.

This chapter was adapted from:
A. Suinesiaputra, L. M. J. Florack, J. J. M. Westenberg, B. M. ter Haar Romeny, J. H. C. Reiber, and B. P. F. Lelieveldt. Optic flow computation from cardiac MR tagging using a multiscale differential method: A comparative study with velocity-encoded MRI. In R. E. Ellis and T. M. Peters, editors, *Medical Image Computing and Computer-Assisted Intervention - MICCAI 2003*, volume 2878 of *Lecture Notes in Computer Science*, pages 483–490. Springer, Nov 2003.

There is an optical illusion about every person we meet.

Essay II – Experience
RALPH WALDO EMERSON

MOTION analysis is becoming increasingly important in cardiovascular imaging. The cine-MR tagging protocol [1] enables the inspection of myocardial motion, because of temporary tag pattern in the myocardium wall. The tag pattern is induced within a tissue, which will follow the tissue deformation. The tissue motion is clearly visible through the deformed pattern.

Automatic reconstruction of a dense velocity field from tagged MRI is the next step toward a detailed cardiac motion analysis. The velocity field can be computed directly by following the apparent pixel movement, which can be derived using optic flow (OF) methods [2]. A large number of different optic flow methods have been proposed (see [3] for a comparison between various OF methods). However, only a few were proposed for extracting the dense OF field from tagged MRI because of one major problem: the *brightness variation* problem.

In the OF computation, a constant pixel intensity is assumed. This is contained in the formulation that a total derivative of the image function L is zero.

$$\frac{dL}{dt} = 0 \quad \text{or} \quad \nabla L \cdot \mathbf{v} = 0;\ \mathbf{v} \in \mathbb{R}^3 \tag{2.1}$$

The MR signal however, linearly depends on the accumulated protons in a certain area. Therefore the tissue deformation causes variation in the pixel intensity due to the divergence of the flow. This chapter presents:

- a new dense optic flow framework, that does not assume a constant pixel intensity, but a constant density. This greatly reduces the sensitivity to brightness variation over time, and therefore enables a more reliable reconstruction of a dense velocity field from tagging MR images, and

- the first direct comparison between reconstructed and directly acquired (using VEC MRI) dense velocity field in clinically representative cases.

The remainder of this chapter is structured as follows. Section 2.1 discusses the proposed approach to the brightness variation problem in tagging MRI and the OF method in detail. In Section 2.2, results from applying the optic flow method to cardiac MR tagging sequences are presented, and statistically compared to the corresponding velocity-encoded (VEC) MR images. Section 4 concludes with a discussion.

2.1 Methodology

2.1.1 Conservation principle in tagging MRI

Let $L : \mathbb{R}^3 \to \mathbb{R}$ be a raw image function and $\mathscr{L}_{\mathbf{v}}$ be the Lie derivative, a generalization notion of the directional derivative of a function, with respect to a spatiotemporal vector $\mathbf{v} \in \mathbb{R}^3$. The optic flow field is defined as a spatiotemporal vector field that satisfies the following constraint

$$\mathscr{L}_{\mathbf{v}}\, L = 0 \tag{2.2}$$

This is called the *Optic Flow Constraint Equation* (OFCE). It defines the mathematical concept of the optic flow field in a more general formulation than (2.1).

Florack et. al. defined two different kind of pixel flows in an image: scalar and density images [4]. In scalar images, the pixel intensity is assumed to be constant. Horn & Schunck's OF equation [2] deals with these images. In density images, the conserved quantity is not a single pixel value, but the intensity is integrated over a local region. Pixel intensities in the density images may vary, but its total integral is conserved: the local "intensity mass" is preserved.

Tagging MRI is a typical example of density images, because the MR signal is formed by the net magnetization of excited protons [5]. The total number of protons in a tissue is preserved, even if the tissue is deformed. Optic flow analysis of tagging MRI therefore greatly benefits from the derivation of OFCE based on the density conservation principle.

Let $L_\rho : \mathbb{R}^3 \to \mathbb{R}$ be a raw image function that holds the density images property. The Lie derivative of L_ρ with respect to a vector $\mathbf{v}$ is defined by taking the derivative of the density function together with the vector field.

$$\mathscr{L}_{\mathbf{v}}\, L_\rho = \sum_{\mu=1}^{3} \partial_\mu \left(L_\rho\, \mathbf{v}^\mu \right) = \nabla \cdot \left(L_\rho\, \mathbf{v} \right) = 0 \tag{2.3}$$

Equation (2.3) is the OFCE definition for the density images. It has an interesting physical interpretation as the divergence of a vector $\mathbf{v}$ representing the rate of expansion per unit volume under the flow. Thus it accounts for the change of volume of the local integrated region. In the next sections, unless stated otherwise, we use the notation of L for the density images.

2.1.2 The First Order Density Multiscale OFCE

Let $\mathbf{v}^T = (w(\mathbf{x}), u(\mathbf{x}), v(\mathbf{x}))$, $\mathbf{x} \in \mathbb{R}^3$ be the optic flow vector, which equals the spatiotemporal vector $\mathbf{v}$ in (2.2), but in a more general form. The function $w : \mathbb{R}^3 \to \mathbb{R}_+$ is the temporal component and $u, v : \mathbb{R}^3 \to \mathbb{R}$ are the spatial components in x and y directions respectively.

As the Lie derivative vanishes in (2.3), its convolution with a Gaussian kernel in the scale-space framework also vanishes. Therefore (2.3) in the Gaussian scale-space framework will be

$$-\int_{\mathbf{R}^3} L\, (\nabla \phi_{\sigma,\tau} \cdot \mathbf{v})\, d\mathbf{x} = 0, \qquad \sigma, \tau \in \mathbb{R}_+ \tag{2.4}$$

where $\phi_{\sigma,\tau}$ is a three dimensional Gaussian kernel with an isotrophic spatial scale σ and a temporal scale τ.

To eliminate the aperture problem [6], an additional constraint is required. Since the exact cardiac motion is not a-priori known, a perpendicular vector to the tangential vector is applied as the additional constraint: the *normal flow* constraint. If $\mathbf{v}^T = (w, u, v)$ is the normal vector, then $\mathbf{v}_t^T = (0, -v, u)$ is its tangential vector. The vectors $\mathbf{v}$ and $\mathbf{v}_t$ can be substituted into (2.4) to get a unique solution.

Another constraint is the *temporal gauge* constraint, which means fixing $w(\mathbf{x}) \rightarrow 1$. This states that there are no creation or elimination of pixel intensities. Using (2.4) for the normal and tangential vector and imposing the temporal gauge condition, the first order OFCE can be defined for the density image. It consists of 8 unknowns (the two components of flow vectors and their derivatives with respect to x, y and t) in 8 linear equations:

$$
\begin{aligned}
-L_t = \;& L_x u + L_y v + \tau^2 L_{xt} u_t + \tau^2 L_{yt} v_t + (L + \sigma^2 L_{xx}) u_x + \sigma^2 L_{xy} v_x + \\
& \sigma^2 L_{xy} u_y + (L + \sigma^2 L_{yy}) v_y \\
-L_{tt} = \;& L_{xt} u + L_{yt} v + (L_x + \tau^2 L_{xtt}) u_t + (L_y + \tau^2 L_{ytt}) v_t + (L_t + \sigma^2 L_{xxt}) u_x + \\
& \sigma^2 L_{xyt} v_x + \sigma^2 L_{xyt} u_y + (L_t + \sigma^2 L_{yyt}) v_y \\
-L_{xt} = \;& L_{xx} u + L_{xy} v + \tau^2 L_{xxt} u_t + \tau^2 L_{xyt} v_t + (2L_x + \sigma^2 L_{xxx}) u_x + \\
& (L_y + \sigma^2 L_{xxy}) v_x + \sigma^2 L_{xxy} u_y + (L_x + \sigma^2 L_{xyy}) v_y \\
-L_{yt} = \;& L_{xy} u + L_{yy} v + \tau^2 L_{xyt} u_t + \tau^2 L_{yyt} v_t + (L_y + \sigma^2 L_{xxy}) u_x + \sigma^2 L_{xyy} v_x + \\
& (L_x + \sigma^2 L_{xyy}) u_y + (2L_y + \sigma^2 L_{yyy}) v_y \\
0 = \;& -L_y u + L_x v - \tau^2 L_{yt} u_t + \tau^2 L_{xt} v_t - \sigma^2 L_{xy} u_x + (L + \sigma^2 L_{xx}) v_x - \\
& (L + \sigma^2 L_{yy}) u_y + \sigma^2 L_{xy} v_y \\
0 = \;& L_{yt} u - L_{xt} v + (L_y + \tau^2 L_{ytt}) u_t - (L_x + \tau^2 L_{xtt}) v_t + \sigma^2 L_{xyt} u_x - \\
& (L_t + \sigma^2 L_{xxt}) v_x + (L_t + \sigma^2 L_{yyt}) u_y - \sigma^2 L_{xyt} v_y \\
0 = \;& L_{xy} u - L_{xx} v + \tau^2 L_{xyt} u_t - \tau^2 L_{xxt} v_t + (L_y + \sigma^2 L_{xxy}) u_x - \\
& (2L_x + \sigma^2 L_{xxx}) v_x + (L_x + \sigma^2 L_{xyy}) u_y - \sigma^2 L_{xxy} v_y \\
0 = \;& L_{yy} u - L_{xy} v + \tau^2 L_{yyt} u_t - \tau^2 L_{xyt} v_t + \sigma^2 L_{xyy} u_x - (L_y + \sigma^2 L_{xxy}) v_x + \\
& (2L_y + \sigma^2 L_{yyy}) u_y - (L_x + \sigma^2 L_{xyy}) v_y
\end{aligned}
\tag{2.5}
$$

L_μ is the image derivative in the Gaussian scale space representation, defined as the convolution of the original image L (as the initial condition) with the Gaussian derivative kernel $\phi_{\sigma,\tau}$ in the μ dimension [7]. Although there are derivatives of each velocity component in (2.5), this chapter only presents the u and v component, as x and y velocity component respectively.

2.1.3 The multiscale scheme

Two parameters are left undefined in (2.5): the scale parameters σ and τ. Although the scale is a free parameter, one proper scale is enough to get a unique solution. Niessen et. al. [8] has studied a scale selection method based on a numerical stability of the solution. The "best result" is defined numerically as the most stable solution of the linear equation system in (2.5). By using the Frobenius norm of the coefficient matrix of (2.5), numerical stable solutions can be estimated.

The next step after solving (2.5) is the *integration of scale space*, which smoothes the output optic flow field [9]. The energy minimization in [9] is modified into the convolution with Gaussian kernels.

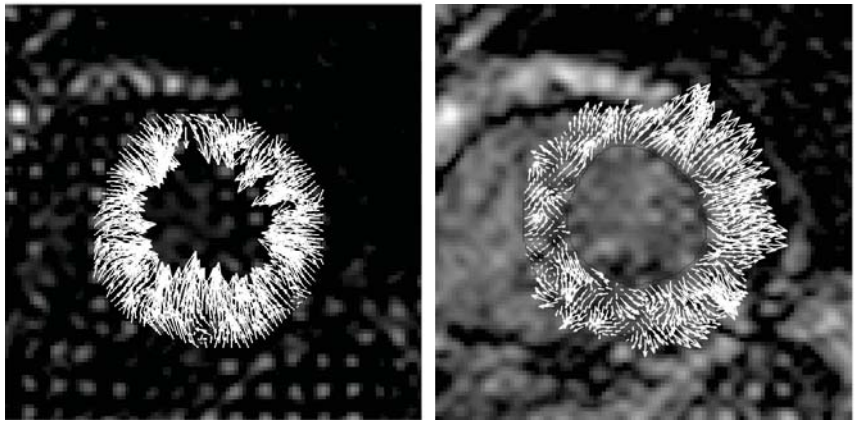

(a) Mid-systole dense OF (b) Mid-diastole dense OF

FIGURE 2.1: One sample comparison result between dense OF from tagging and VEC MRI.

Let $\tilde{\mathbf{v}}(\mathbf{x}), \mathbf{x} \in \mathbb{R}^3$ be an optic flow vector after the integration and $\mathbf{v}_{\sigma,\tau}(\mathbf{x})$ be an optic flow vector after the computation of (2.5) with spatial scale σ and temporal scale τ. The notion of σ,τ in the vector $\mathbf{v}$ is added to incorporate the scale selection scheme. The integration of scale space is given by the following convolution process:

$$\tilde{v}^{\mu}(\mathbf{x_0}) = \int_{\mathbf{x}\in\mathbb{R}^3} p(\mathbf{x_0})\, v^{\mu}_{\sigma,\tau}(\mathbf{x_0}) \phi_{\sigma,\tau}(\mathbf{x}-\mathbf{x_0})\, d\mathbf{x} \tag{2.6}$$

where μ is one of vector's components, $p(\mathbf{x})$ is a penalty function and $\phi_{\sigma,\tau}(\mathbf{x})$ is the Gaussian kernel. The penalty function $p(\mathbf{x})$ in (2.6) is defined as:

$$p(\mathbf{x}) = \exp\left(-\frac{\lambda\, \kappa(\mathbf{x})}{N_{\kappa}}\right) \tag{2.7}$$

where $\kappa(\mathbf{x})$ is the Frobenius norm of the coefficient matrix of (2.5) at the spatiotemporal position $\mathbf{x}$. The value λ is a constant in the range of (0..1] and N_{κ} is a normalization factor. The value of (2.7) decreases exponentially when κ is large, which means that the more unstable solution contributes less in the final optic flow result.

2.2 Experimental results

The multiscale OF method for tagged MRI has been tested and validated on several analytical images and tagging MRI of a phantom agar [10]. In this chapter, the method is applied to real cardiac tagged MR images from a number of cardiac-healthy subjects. The OF method is restricted to estimate only for in-planar motion (2D) in tagging MRI. The results are compared to directly acquired VEC MRI.

TABLE 2.1: Correlation coefficients

Components	Full cycle	Systolic	Diastolic
Radial	$r = 0.86$ ($SD = 0.04$)	$r = 0.98$ ($SD = 0.01$)	$r = 0.71$ ($SD = 0.13$)
Circumferential	$r = 0.42$ ($SD = 0.17$)	$r = 0.52$ ($SD = 0.18$)	$r = 0.23$ ($SD = 0.29$)

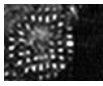

2.2.1 Clinical Data

Eight healthy volunteers were selected without history of valvular disease, proven from echocardiography. VEC MR images were acquired in a short-axis orientation at a mid-ventricular level. A standard spoiled gradient-echo was applied with velocity-encoding in three directions (maximal velocity sensitivity is 20 cm/s). Retrospective gating with delayed reconstruction was used to cover the full cardiac cycle (30 phases). This acquisition was performed during free breathing.

An MR tissue tagging sequence is used in the same short-axis orientation and position for comparison. Rectangular grid tagging is performed with tag grid spacing = 8.3 mm. Prospective triggering is used with maximum number of heart phases reconstructed, resulting in typical 20-30 phases during one cardiac cycle. This acquisition is performed under breath-holding (in expiration).

Both the VEC and tagging MR images for all patients were acquired in the same study time, with same patient positioning. Due to different breathing conditions, the left ventricular (LV) contours were drawn separately. Contours for tagging images were drawn manually using a dedicated cardiac MR analytical software package (MASS, v5.0, Medis, Leiden, the Netherlands [11]). Contours were drawn in the regular short-axis image, at the closest slice position to the tagging image, because of the better visibility of the myocardial contours in (non-tagged) short-axis slices. Contours for the VEC MRI were drawn manually in the through-plane velocity image, because it gives clearer definition of the myocardial wall than the in-plane velocity images.

In the analysis, time phases of tagging and VEC sequences were normalized into a single cycle. Since the number of phases in tagging images was not equal, MR tagging images were interpolated 30 time frames according to the time steps in the VEC MRI.

2.2.2 Results

The region of interest is the LV myocardium. Figure 2.1 and Figure 2.2 shows one sample result of the OF field from a subject compared visually with their corresponding VEC MR images at mid-systole and mid-diastole phases. Only vectors inside the LV myocardium are shown. Notice how the tagging patterns are fading at later phases.

For this comparison between VEC MRI and the computed OF from tagging, only the in-plane motion of the VEC MRI was analyzed. Therefore the z-velocity components were discarded. The comparison is focused at the global LV wall motion, instead of regional wall motion, because the scope of this paper is to investigate how the LV wall motion from optic flow globally relates to VEC MRI.

(a) Mid-systole VEC (b) Mid-diastole VEC

FIGURE 2.2: One sample comparison result between dense OF from tagging and VEC MRI.

The LV wall undergoes two basic motions, i.e. radial and circumferential components. The radial component defines contraction motion relative to the center of the LV, while the circumferential defines the torsion movement. Figure 2.3 shows the comparison of the mean global radial and circumferential velocity components between the computed OF and VEC MRI.

The correlation coefficient for each components were calculated to investigate the relation between the OF and VEC MRI. As can be seen in Figure 2.4, the OF and the VEC radial velocity has high correlation ($r = 0.86$). This is not the case for the circumferential velocity ($r = 0.42$). Also the radial velocity correlates better at the systolic part of the cycle, while the diastolic half (second half cycle) is less correlated (Table 2.1). In the scatter plot (Figure 2.4), this phenomenon is shown by a cluster of systolic plots (asterisk signs) and diastolic plots (plus signs).

2.3 Discussion

The circumferential component correlates less good ($r = 0.42$). This can be explained by two factors. The circumferential movements in the VEC images are more visually apparent than the circumferential movements in the tagging images. This may be caused by the longer trigger delay time of the tagging images, i.e. the rapid torsion at the start of the contraction is not sufficiently covered by the tagging sequence. Therefore the optic flow method is unable to produce the motion that is not sufficiently present in the image data.

Moreover the aperture problem was solved using the normal flow constraint, which reduces all pixel motions to be in the direction of the image gradient. In order to over-

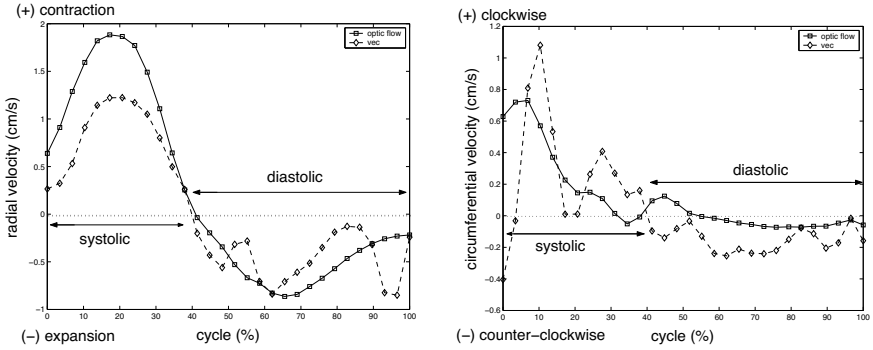

FIGURE 2.3: Mean of global radial (left) and circumferential (right) components from 8 subjects.

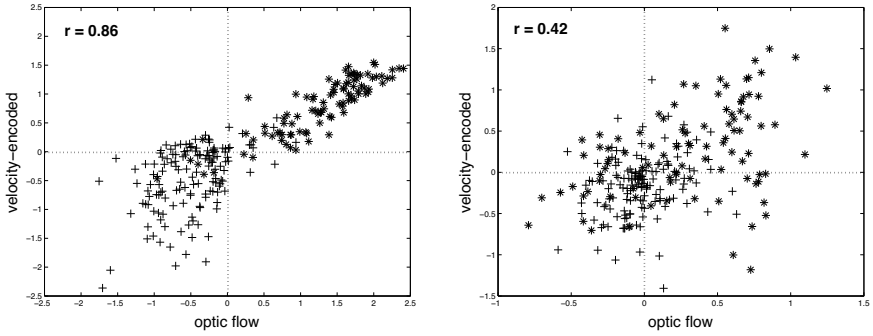

FIGURE 2.4: Scatter plot of radial (left) and circumferential (right) component. Asterik ('*') signs are the systolic part, while plus ('+') signs are the diastolic part.

come this limitation, the normal flow constraint should be replaced by a more knowledge-driven motion constraint. If a-priori knowledge of the LV wall motion is integrated, for instance taking into account the torsion movement, then it would be better to replace the normal flow constraint with this knowledge.

The computed dense OF field from tagged MRI shows a very good correlation with the VEC MRI for the LV wall radial contraction. Especially in the systolic part of the cardiac cycle this correlation is stronger ($r = 0.98$ in systole and $r = 0.71$ in diastole). In most cases, the cardiac systolic function is clinically more meaningful than the diastolic part. Systolic function gives information of how well the heart can pump the blood to the whole body. Based on this observation, the proposed dense OF method shows a promising non-invasive technique to assess the velocity field during the systolic part of the cardiac cycle.

The proposed method has the flexibility to be extended to 4D by adding one more spa-

tial component in the spatiotemporal vector definiton. The optic flow equations would become more complex and more additional constraint equations are needed.

2.4 References

[1] L. Axel and L. Dougherty, "MR imaging of motion with spatial modulation of magnetization," *Radiology*, vol. 171, no. 3, pp. 841–5, Jun 1989.

[2] B. K. P. Horn and B. G. Schunck, "Determining optical flow," *Artif. Intell.*, vol. 17, no. 1-3, pp. 185–203, 1981.

[3] S. S. Beauchemin and J. L. Barron, "The computation of optical flow," *ACM Comput. Surv.*, vol. 27, no. 3, pp. 433–467, 1995.

[4] L. M. J. Florack, W. J. Niessen, and M. Nielsen, "The intrinsic structure of optic flow incorporating measurement duality," *International Journal of Computer Vision*, vol. 27, no. 3, pp. 263–286, 1998.

[5] W. R. Nitz and P. Reimer, "Contrast mechanisms in MR imaging," *Eur Radiol*, vol. 9, no. 6, pp. 1032–46, 1999.

[6] D. Marr, *Vision*. San Fransisco: W.H. Freeman & Co., 1982.

[7] T. Lindeberg, *Scale Space Theory in Computer Vision*. Dordrecht: Kluwer Academic, 1994.

[8] W. Niessen and R. Mass, "Optic flow and stereo," in *Gaussian Scale-Space Theory*, J. Sporring, Ed. Kluwer, 1997, pp. 31–42.

[9] K. S. Pedersen and M. Nielsen, "Computing optic flow by scale-space integration of normal flow," in *Scale-Space and Morphology in Computer Vision*, ser. Lecture Notes in Computer Science, M. Kerckhove, Ed., vol. 2106. Springer, 2001, pp. 14–25.

[10] A. Suinesiaputra, "Multiscale optic flow analysis for magnetic resonance tagging," Department of Biomedical Engineering, Technische Universiteit Eindhoven, BMT-Report 2002-01, Jan. 2002.

[11] R. J. van der Geest, V. G. Buller, E. Jansen, H. J. Lamb, L. H. Baur, E. E. van der Wall, A. de Roos, and J. H. Reiber, "Comparison between manual and semiautomated analysis of left ventricular volume parameters from short-axis MR images," *J Comput Assist Tomogr*, vol. 21, no. 5, pp. 756–65, 1997.